

# THE APPLICATION OF PYRAMID LUCAS-KANADE OPTICAL FLOW METHOD FOR TRACKING RAIN MOTION USING HIGH-RESOLUTION RADAR IMAGES

Roby Hambali<sup>a\*</sup>, Djoko Legono<sup>b</sup>, Rachmad Jayadi<sup>b</sup>

<sup>a</sup>Department of Civil Engineering, Universitas Bangka Belitung, Kampus Terpadu UBB, Bangka, Indonesia

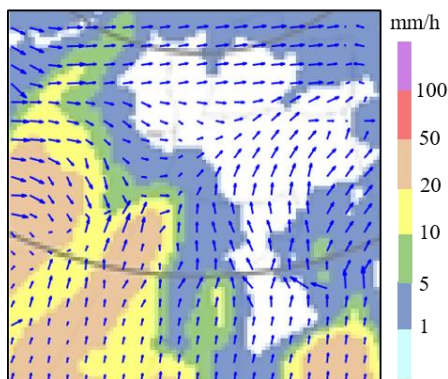
<sup>b</sup>Department of Civil and Environmental Engineering, Universitas Gadjah Mada, JL. Grafika No. 2, Yogyakarta, Indonesia

## Article history

Received  
16 December 2019  
Received in revised form  
30 November 2020  
Accepted  
3 December 2020  
Published online  
17 December 2020

\*Corresponding author  
roby.hambali@mail.ugm.ac.id

## Graphical abstract



## Abstract

Short-duration rainfall characteristics in the form of certain intensity, time, and spatial distribution become valuable contribution for lahar flow disaster mitigation in a mountainous region. Due to mitigation purpose, such information can be provided through the rainfall nowcasting process. One of the promising rainfall nowcasting applications is the extrapolation-based method. Rain motion tracking is a crucial part of the rainfall nowcasting based on this method. This paper discusses the application of Pyramid Lucas-Kanade Optical Flow (PLKOF) method on the rain motion tracking analysis using 150x150m resolution radar image. The study of rain motion tracking is carried out using 112 successive rainfall images with 10-minutes time interval originating from Mt. Merapi X-band multiparameter radar. The rainfall movement patterns in short duration are presented in the displacement vector (u,v) images and scatter diagrams of rain motions at x- and y-directions. From the simulations, it was found that the average displacement of rain motions in the Mt. Merapi region is 9 pixels (8.3 km/h) with the dominant direction is northeast. The results show that PLKOF is relatively good at detecting small displacements, yet unable to identify the occurrence of rain growth and decay properly. The ability of PLKOF method in predicting the position of rain cell displacement is satisfied as indicated by the POD, CSI, and FAR indexes.

**Keywords:** Rain motion, displacement vector, optical flow, nowcastig, X-band MP radar

© 2021 Penerbit UTM Press. All rights reserved

## 1.0 INTRODUCTION

Mt. Merapi is one of the most active volcanoes in Indonesia and spouting large amounts of volcanic materials in every eruption. The eruption might pose a severe threat to the communities and the environment. There are three types of disasters that may be produced by Mt. Merapi, and these include (1) pyroclastic flows; (2) volcanic ashfall; and (3) lahar flows as triggered by heavy rainfall [1]. The latest

seems to be affected by rainfall behavior at the flank area of the mountain. According to Lavigne *et al.*, rainfall intensity as measured over 1-hour or 10-minute intervals play a crucial role in triggering lahar flows [2]. Therefore, information of the spatial distribution of rainfall intensity for short duration is highly worthwhile for applications those related to the mitigation of lahar flows disaster [3]. To anticipate lahar flow disasters and define rainfall criteria that induce lahar flows, monitoring of hydraulic and hydrological parameters is

needed, both in historical and real-time data [3, 4]. The results of the monitoring can be used to predict the occurrence of lahar flows. Through the Indonesia-Japan research collaboration of SATREPS Project, an X-band multi-parameter (X-band MP) radar rainfall has been operated since October 2015 to complement existing hydrological monitoring devices surrounding Mt. Merapi. Figure 1 shows a map of study area covered rainfall monitoring device network at Mt. Merapi region, including automatic rainfall recorder (ARR) and X-band MP radar. To this time, Mt. Merapi X-band MP radar has not been utilized for rainfall nowcasting purposes. The establishment of an appropriate rainfall nowcasting model will undoubtedly give a valuable contribution to the lahar flows disaster mitigation system in Mt. Merapi region.

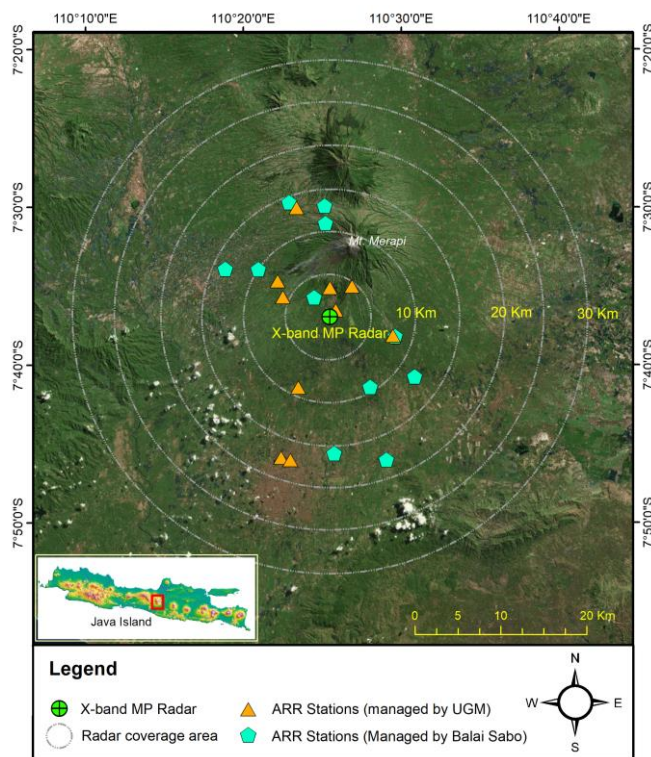


**Figure 1** The study area in the Mt. Merapi region

Various short-term rainfall nowcasting methods have been developed by many researchers in the past few decades, both through simple approaches to those with high complexity. At present, only two applications are potentially used for rainfall nowcasting, namely Numerical Weather Prediction (NWP) and the Extrapolation method [5, 6]. Both of the models use different approaches, but complement each other because it has strengths and weaknesses [7, 8]. The NWP model has a limitation of short lead time prediction due to sensitivity to assimilation algorithms, initial conditions, and spatial resolution [6, 9–11]. Also, the model is unsatisfying for some applications because the coarse spatial resolution of

the output model often misses sub-grid scale processes such as small cells convective activity [6]. Compared to the NWP model, extrapolation-based methods offer better results for rainfall nowcasting [6, 8, 11, 12], especially in the first few hours of storm events [7, 13]. Recently, Bechini and Chandrasekar [13] found that extrapolation-based methods provide good results for the lead time up to about 20 minutes.

The underlying idea of the extrapolation method is connecting two successive images to determine rain motion and extrapolate the distribution of values in the future [15]. There are usually two main processes in the extrapolation-based of rainfall nowcasting algorithm, and those are tracking and forecasting [8, 11]. In general, motion tracking techniques are divided into two types; those are object-based and pixel-based tracking. Object-based tracking uses image perspective and consider storm events as individual objects. However, it has difficulty tracking small-scale storms and rapidly developing cloud-patches [8, 15]. The pixel-based algorithm considers the motion between two consecutive radar images. This method has been used widely to improve the short-term predictability of storms using high-resolution radar data [8, 11, 15–20].

One of the very promising pixel-based methods is optical flow (OF). Several previous studies on rainfall nowcasting models that discussed the application of optical flow methods in the motion tracking process are [8, 12, 15, 16, 19, 20]. Those studies show that motion tracking using an optical flow method superior compared to other methods, even though it is applied to varying nowcasting models and nature of data. However, of all these investigations, none of them has used very high spatial resolution data similar to the Mt. Merapi X-band MP radar. Therefore, this study attempt to apply optical flow in rain motion tracking analysis using 150x150m resolution X-band MP radar image. With the smaller pixel size, the analysis on the sub-pixel level does not need to be utilized and more accurate rain motion estimation are obtained.

## 2.0 METHODOLOGY

### 2.1 Mt. Merapi X-band MP Radar

The X-band radar is now widely used to estimate more accurate rainfall intensity with higher object resolution. It has several advantages compared to the previous generation of rainfall radar, involving higher spatial and temporal resolution, smaller antenna size, easier mobility due to smaller antennas for the same beam width, and lower costs [24].

In order to provide a decision support system to reduce the impact of Mt. Merapi multimodal sediment disaster, an X-band polarimetric multi-parameter radar was installed on the rooftop of Mt. Merapi museum at 742 m above MSL through the SATREPS Project for integrated study on mitigation of multimodal disasters caused by ejection of volcanic products. This radar is

classified as a short-range radar with an operating frequency of 9470 MHz and the maximum range of 30 km, to produces data output in the form of reflectivity factor ( $Z_H$ ), Doppler velocity ( $V$ ), Doppler velocity spectrum width ( $W$ ), cross polarization difference phase ( $\varphi_{dp}$ ), specific differential phase ( $K_{DP}$ ), corporal correlation coefficient ( $\rho_{HV}$ ), differential reflectivity ( $Z_{DR}$ ), and rainfall intensity ( $R$ ). Currently, the X-band MP radar is being utilized for rainfall monitoring around the Mt. Merapi region with a 2-minute temporal resolution.

Mt. Merapi X-band MP Radar uses Plan Position Indicator (PPI) scanning mode to detect rainfall, with elevation angles of 3, 5, 7, 9, 11, 13, 15, 18, and 21°. It generates a 150x150 m spatial resolution for each pixel. Table 1 shows the specifications of the Mt. Merapi X-band MP radar system. The rainfall rates are

estimated using a composite algorithm as proposed by Park *et al.* [24] based on the reflectivity ( $Z$ ) and specific differential phase ( $K_{DP}$ ) of CAPPI (constant altitude plan position indicator) at 1500 m height.

For  $K_{DP} \leq 03^\circ\text{km}^{-1}$ ,

$$R(Z_H) = 7.07 \times 10^{-3} Z_H^{0.819} \quad (1)$$

For  $K_{DP} > 03^\circ\text{km}^{-1}$ ,

$$R(K_{DP}) = 19.63 K_{DP}^{0.823} \quad (2)$$

**Table 1** The specifications of the Mt. Merapi X-band MP Radar system [25]

Polarization	Dual polarimetry (vertical and horizontal), simultaneously transmitted/received
Operating Frequency	9470 MHz
Power Supply	100-240 VAC, Single phase, 50/60 Hz
Power Consumption	Max 350 W
Beam Width	2.7°
Peak Output Power	100 W
Horizontal Scan Angel	360°
Vertical Scan Angel	-2° to 90°
Resolution of Angel	0.1°
Antenna Rotation Speed	0.5 to 16 rpm
Radome size	1086 mm (diameter) x 1024 mm (height)
Aperture Size	750 mm (diameter)
Maximum Range	30 km
Scan Modes	PPI, CAPPI, RHI (Sector scan available)
Output Data	Reflectivity factor $Z_H$ (dBZ), Doppler velocity $V$ (m/s), Doppler velocity spectrum width $W$ (m/s), Cross polarization difference phase $\varphi_{dp}$ (deg), Specific differential phase $K_{DP}$ (deg/km), Corporal correlation coefficient $\rho_{HV}$ , Differential reflectivity $Z_{DR}$ , Rainfall intensity $R$ (mm/h)
Data Correction	Distance attenuation, Rain attenuation, Excessive Doppler velocity, Suppression of signal return from land, Clutter suppression

## 2.2 Motion Tracking Using Optical Flow

Optical flow is an image processing technique in the field of computer vision. Horn and Schunck [26] state that optical flow is the distribution of the movement velocity of the brightness pattern in the image. The concept of optical flow was first introduced by Gibson [27] to describe the visual stimulus given to the movement of animals throughout the world. This method then developed for research purposes in various fields. In hydrology, optical flow is one of the promising techniques for several applications. For instance, Tauro *et al.* [28] proposed a differential local optical flow-based approach through optical tracking velocimetry (OTV) to estimate the surface flow velocity field of natural streams. Lenzano *et al.* [29] used large displacement optical flow (LDOF) algorithm to obtain surface movement data to derive ice flow velocities in a glacier based on

terrestrial, monoscopic time-lapse image series. An investigation on the short-term forecast of the effective cloud albedo based on TV-L<sup>1</sup> optical flow estimation methods was conducted by Urbich *et al.* [30]. In this investigation, TV-L<sup>1</sup> method is used for calculating cloud motion vectors. Hadhri *et al.* [31] introduced a framework for the tracking of geophysical complex phenomena via robust pre-processing steps and optical flow computing based on time-lapse images. This framework was proposed to overcome the existing techniques for automatically estimating accurate long term motion time series. For rainfall nowcasting purpose, Ayzel *et al.* [32] introduced the open software "rainymotion" as a benchmark for radar-based precipitation nowcasting. Different optical flow algorithms are used for tracking step in this model.

Optical flow analysis aims to calculate the approximate of the motion field based on image

intensity [33]. The basic assumption of optical flow calculations is that the brightness of an image is considered constant on an object [34]. It can be explained that if an object position changed (displaced) in a short time interval  $t_1$  to  $t_2$ , its reflectivity and intensity would remain. In mathematical expression, the above assumption can be written as follows.

$$f(x + \Delta x, y + \Delta y, t + \Delta t) \approx f(x, y, t) \tag{3}$$

$f(x, y, t)$  is the intensity of the image at position  $(x, y)$  in time  $t$ ,  $\Delta x$  and  $\Delta y$  are displacements, while  $\Delta t$  is the time interval between successive images. In order to be able to analyze the motion of the object in numerical computation, Taylor series expansion should be applied. Since the change in a position considered small, then the higher order terms of Taylor series expansion are ignored. The Eq. (3) then re-written as Eq. (4).

$$f(x + \Delta x, y + \Delta y, t + \Delta t) = f(x, y, t) + \frac{\partial f}{\partial x} \Delta x + \frac{\partial f}{\partial y} \Delta y + \frac{\partial f}{\partial t} \Delta t + O \tag{4}$$

where  $\frac{\partial f}{\partial x}$ ,  $\frac{\partial f}{\partial y}$ , and  $\frac{\partial f}{\partial t}$  are the partial derivatives of the image function in  $x$ ,  $y$  and  $t$  dimensions, while  $O$  is a negligible error value. If Eq. (3) is substituted to Eq. (4), we get

$$f(x, y, t) = f(x, y, t) + \frac{\partial f}{\partial x} \Delta x + \frac{\partial f}{\partial y} \Delta y + \frac{\partial f}{\partial t} \Delta t \tag{5}$$

$$\frac{\partial f}{\partial x} \Delta x + \frac{\partial f}{\partial y} \Delta y + \frac{\partial f}{\partial t} \Delta t = 0 \tag{6}$$

In order to find the velocity variable, then all terms in Equation (6) are divided by  $\Delta t$ , so that the equation becomes

$$\frac{\partial f}{\partial x} \frac{\Delta x}{\Delta t} + \frac{\partial f}{\partial y} \frac{\Delta y}{\Delta t} + \frac{\partial f}{\partial t} = 0 \tag{7}$$

$$\frac{\partial f}{\partial x} u + \frac{\partial f}{\partial y} v + \frac{\partial f}{\partial t} = 0 \tag{8}$$

where  $u$  and  $v$  are the displacement velocity in the  $x$  (west-east) and  $y$  (north-south) directions. The function described is a value of brightness or intensity, so then it will be written in the form of the following optical flow constraint equation.

$$I_x u + I_y v + I_t = \nabla I v_m + I_t = 0 \tag{9}$$

$\nabla I = (I_x, I_y)$ , is a spatial gradient, while variable  $v_m = (u, v)$  is the optical flow vector that should be searched.

The equation (9) provides only the component of the vector in the direction of the spatial gradient. This situation remains a significant problem called the aperture problem. The aperture problem refers to the ambiguity of the inferred global motions when the observing local image structures which only vary along one direction [35]. Since the flows are calculated from individual pixels, we are limited by the size of the gradient operators. Therefore, it might be too small to see the other component of the optical flow vector. The aperture problem of the optical flow can be solved by Lucas-Kanade method that utilized a local differential approach to calculate the movement of the pixel. In this method, the movement of optical flow in adjacent pixels is assumed to be constant [16] as illustrated by blue arrows in Figure 2.

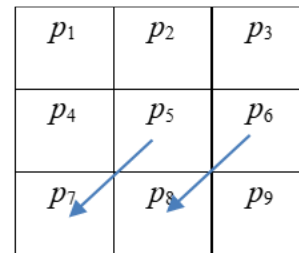


**Figure 2** The basic assumption of optical flow in the Lucas-Kanade method

Based on the above assumptions, Equation (9) can be rewritten as

$$I_x(p) u + I_y(p) v = -I_t(p) \tag{10}$$

In the form of a matrix, equation (10) is written as follows.

$$\begin{bmatrix} I_x & I_y \end{bmatrix} \begin{bmatrix} u \\ v \end{bmatrix} = -I_t \tag{11}$$

$$A = \begin{bmatrix} I_x & I_y \end{bmatrix} \tag{12}$$

$$A A^T = B = \begin{bmatrix} I_x I_x & I_x I_y \\ I_y I_x & I_y I_y \end{bmatrix} \tag{13}$$

Then Equation (13) is substituted into Equation (12), resulting in equation (13).

$$B \begin{bmatrix} u \\ v \end{bmatrix} = -A^T I_t \tag{14}$$

$$\begin{bmatrix} I_x I_x & I_x I_y \\ I_y I_x & I_y I_y \end{bmatrix} \begin{bmatrix} u \\ v \end{bmatrix} = \begin{bmatrix} -I_x I_t \\ -I_y I_t \end{bmatrix} \tag{15}$$

The value of  $u$  and  $v$  can be calculated by multiplying all sides by inverse matrix of  $[B]^{-1}$ . So that the equation becomes

$$\begin{bmatrix} u \\ v \end{bmatrix} = \begin{bmatrix} I_x I_x & I_x I_y \\ I_y I_x & I_y I_y \end{bmatrix}^{-1} \begin{bmatrix} -I_x I_t \\ -I_y I_t \end{bmatrix} \tag{16}$$

Equation (16) can be solved by applying a Gaussian convolution (Equation 17) so that the data noise can be filtered.

$$\begin{pmatrix} u \\ v \end{pmatrix} = \begin{pmatrix} g(x) * (I_x I_x) & g(x) * (I_x I_y) \\ g(x) * (I_y I_x) & g(x) * (I_y I_y) \end{pmatrix}^{-1} \begin{pmatrix} -g(x) * (I_x I_t) \\ -g(x) * (I_y I_t) \end{pmatrix} \tag{17}$$

where  $*$  denotes convolution operations, and  $g(x)$  is a Gaussian kernel.

The Lucas-Kanade method has limitations in tracking fast-moving objects and large-scale movement due to the optical flow constraint equation [16]. The application of the Gaussian image pyramid technique can get over such limitation [9]. The Gaussian image pyramid is a data structure that reconstructs images by convolving Gaussian kernel to the image through reduced image representation [19, 33, 34]. This method can efficiently extract features of different scales. In order to connect multiscale features, each level of the Gaussian pyramid image is normalized by the spatial interpolation. This step is carried out until the spatial size is as large as the original image at the first level. Typical construction of Gaussian image pyramid decomposition is shown in Figure 3.

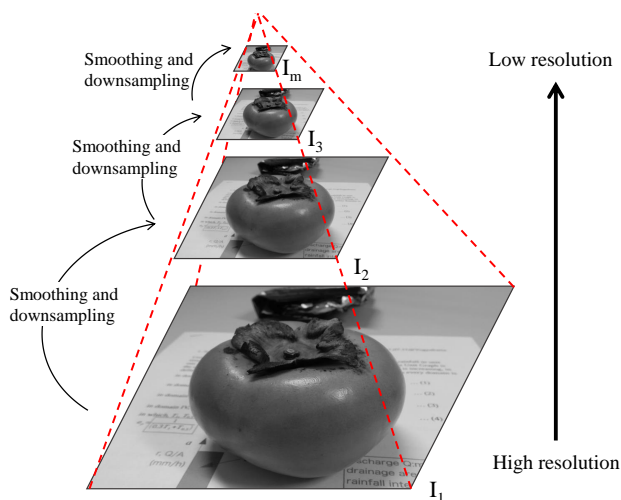


Figure 3 The constructs of Gaussian image pyramid decomposition (modified after [38])

The concept of the Pyramid Lucas-Kanade Optical Flow (PLKOF) method [9] is presented in Figure 4. Figure 4 illustrates two consecutive images at time  $t - \Delta t$  and  $t$  are used to estimate the displacement vector of rain motions. At time  $t - \Delta t$  (Figure 4a) there are six rainy pixels, namely  $q_{28}$ ,  $q_{29}$ ,  $q_{36}$ ,  $q_{37}$ ,  $q_{45}$ , and  $q_{46}$ . Next, at time  $t$  (Figure 4b), there was an expansion of rainy pixels to the northwards, westwards, and northwestwards from the previous time, so that becomes 12 rainy pixels. The displacement vectors of rain motions are estimated based on those spatial changes (Figure 4c). The solid arrows are the displacement vector of rain motion which is estimated from time  $t - \Delta t$  to time  $t$ , while the dot arrows are the prediction of the displacement vector of rain motions at time  $t + \Delta t$ .

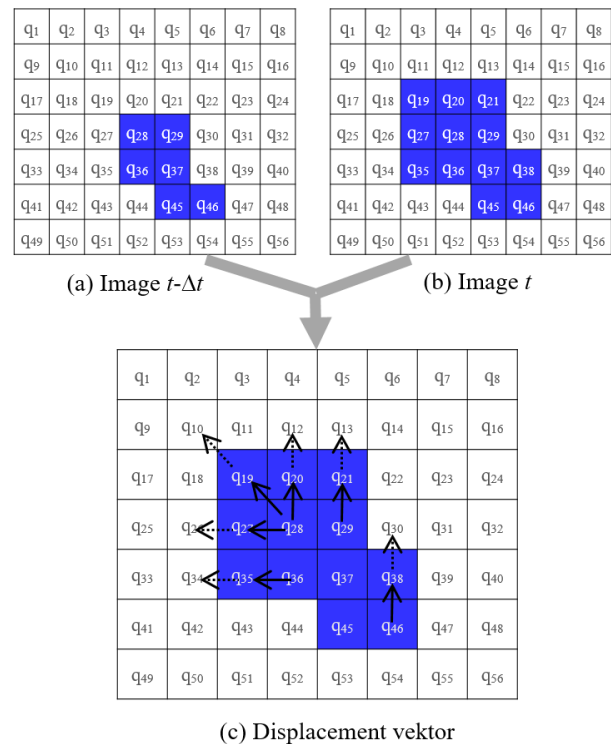


Figure 4 The concept of motion tracking using PLKOF method (modified after [9])

The advantage of PLKOF technique is its ability to detect large and small displacement motions using a multi-resolution data structure. There are two steps to implement the Gaussian image pyramid: first, applying Gaussian smoothing on the images; second, down-sampling the image to obtain the resampled images. The application of image smoothing is intended to enhance the robustness of the optical flow against noise contained in the image, while the down-sampling process is designed to deal with the search of objects at different scales efficiently. In order to generate the smoothed images, the original rainfall images can be convolved with a Gaussian Kernel,  $g(x)$ . The Gaussian kernel is one of the most commonly used kernels in

the image smoothing process, for example by [8, 19, 35–38]. One of the Gaussian kernel size that has been used by Barron *et al.* [39] and Neustaedter [42] in optical flow analysis are 1/12 [-1 8 0 -8 1].

### 2.3 Case Study

In this study, 112 consecutive images of 9 rainfall events during 2016-2018 were selected to be analyzed (Table 2). The rainfall events were selected randomly neglecting the speed of the rain movement, due to limited data availability. These events have an evenly distributed rainfall in radar coverage areas with varied intensity. The images used in this study are produced based on quantitative precipitation estimation (QPE) algorithm of Mt. Merapi X-band MP Radar (Figure 5). The size of each image is 600x600 pixels, coverage geographical area from 110°9'18"E-110°42'0"E Longitude and 7°21'30"S-7°53'28"S. Considering the consumption of sufficiently long computing time for high-resolution images (pixel size 150x150 m), this rain motion tracking analysis is performed only in the domain of 100x100 pixels with 10-minutes time interval.

**Table 2** The list of rainfall events collected in the analysis

Rainfall events (yyyymmdd)	ID	Start time (hh:mm)	Number of images	Rainfall intensity (mm/h)	
				Max	Avg.
20161110	R1	13:00	22	107.4	9.14
20161230	R2	04:20	13	70.1	4.44
20170105	R3	14:30	10	112.5	10.4
20171008	R4	16:40	9	106.8	6.8
20171220	R5	13:30	19	113.5	9.4
20171226	R6	16:30	12	114.5	14.7
20180204	R7	13:40	6	106.3	9.1
20180211	R8	14:40	7	89.6	10.6
20180307	R9	13:30	14	117.8	13.6

Figure 5 is an example of 30 minutes of consecutive images on January 5, 2017, to show the spatial change of short-duration rainfall in the Mt. Merapi region. Visually, it can be seen the changes of rainfall field and intensity every 10 minutes from these consecutive images, where high-intensity rainfall (>20 mm/h) increasingly widespread towards the south-west (SW) and north-west (NW) directions. Indeed, the rainfall around Mt. Merapi is highly dynamics, both spatially and temporally. It is indicated by the high variability of spatial and temporal distribution in short duration.

The shadow areas observed in the southwest and northeast parts (Figure 5) are due to beam shielding related to the radar position which was too close to the tower building (southwest) and Mt. Merapi

summit (northeast). The radar elevation was relatively low to avoid these obstacles.

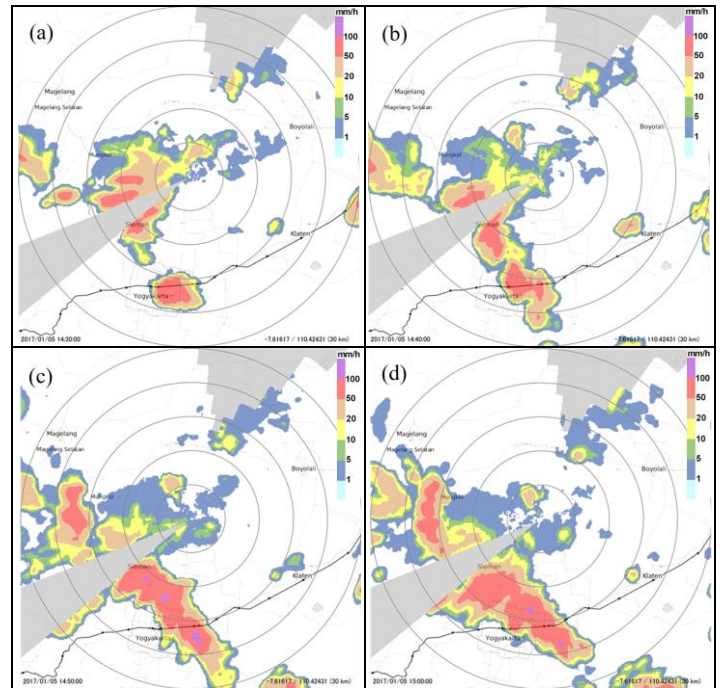


**Figure 5** Mt. Merapi X-band MP Radar images on January 5th, 2017 at (a) 14:30, (b) 14:40, (c) 14:50, and (d) 15:00

Three levels of pyramid images were used in the analysis, which the original image is at the bottom level. We applied the Gaussian pyramid with down-sampling two consecutive images to half size in each level (except original images), recursively from high resolution to low resolution. The values of the optical flow in the initial level are obtained by computing the sub-pixel value using bilinear interpolation method between integers pixel at each level. Minimum threshold of rain motion velocity for recursive process of optical flow calculation is determined 0.01.

The analysis results are presented in the displacement vector map and scatter diagrams of rain motion, which describe the magnitude and directions. The value of displacement vectors explained by average and dominant directions. Refers to Urbich *et al.* [30], the calculation of rain motion vectors is based on the minimization of the absolute difference between a shifted image in the x-y direction and the subsequent image. Therefore, the performance of PLKOF method for rain motion tracking in this study is evaluated through its ability in rain position predictability at time  $t+\Delta t$ . The predictability indexes are POD (probability of detection), FAR (false alarm ratio) and CSI (critical success index), and defined as

$$POD = \frac{hits}{hits + misses} \tag{16}$$

$$FAR = \frac{\text{false alarms}}{\text{hits} + \text{false alarms}} \tag{17}$$

$$CSI = \frac{\text{hits}}{\text{hits} + \text{misses} + \text{false alarms}} \tag{18}$$

A contingency table is given (Table 3) to verify hits, false alarm, and misses. Contingency table is a two-dimensional table that provides a discrete distribution of forecast and observation values in terms of pixels number.

**Table 3** Contingency table for events verification

Forecast	observation	
	Yes	No
Yes	hits	false alarms
No	misses	correct negatives

POD is the number of hits divided by the total number of observed events. Physically, it means event was forecast and it occurred. FAR is the number of false alarms divided by the number of predicted events. In other words, FAR mean event was forecast but did not occur. Critical success index (CSI) is a simple summary statistic that combines information from hits, misses, and false alarms. The POD, FAR and CSI score range from 0 to 1 with the best score of 1 for POD and CSI, and 0 for FAR.

### 3.0 RESULTS AND DISCUSSION

This study has confined the discussion to the process of rain motion tracking carried out using the PLKOF method. All critical stages in the rain motion tracking process based on X-band MP radar images have been performed. From 112 images that have been analyzed, it shows that the selected rainfall events have diverse temporal and spatial characteristics. Most of the rainfall events have a reasonably tidy change in spatial distribution with low to moderate rain motion (3.6-7.2 km/h), such as the rainfall events of 10 November 2016, 30 December 2016, 5 January 2017, 8 October 2017, 26 December 2017, and 11 February 2018. As an example, on 5 January 2017, rainfall shows the position change steadily and slowly from southwest to northeast, then rain growth occurs at the southern part and moves to the northeast. Some rainfall events have a rapid change (> 7.2 km/h), and others experience unrest in directions change, such as the rainfall events on 26 December 2016 and 7 March 2018.

Figure 6 shows an example of motion vector estimation with 10 minutes interval for the case study on 10 November 2016. At 14:20-14:30 LT (Figure 6a and 6b), the displacement vectors of rainfall moving from south and west to the northeast with average displacement value is 7 pixels or equal to 6.3 km/h in velocity, and maximum displacement is 27 pixels

(equivalent to 24.3 km/h). At 14:30-14:40 LT (Figure 6c and 6d), the displacement vectors of rain motion show a dominant component on the right side domain area moving from south (S) to the north (N) and northwest (NW). Average displacement values are 4 pixels (3.6 km/h), while the maximum displacement is 18 pixels (16.2 km/h).

To set better understand the quantification of the displacement vector of rain motion in the x-direction (east-west) and y-direction (north-south), scatter diagrams have been used. Figure 7 and Figure 8 depict the scatter diagrams of the displacement vector of rain motion for rainfall events on 10 November 2016, as shown in Figure 6. Based on Figure 7, it can be explained that the dominant direction of rain motion is northward, although some large displacements appeared to point northeast. Not so much different from the previous case, Figure 8 also shows the dominant direction as same as Figure 7. Nevertheless, in this case, the rain motions relatively concentrated to the northwest, and only small portions are heading in the opposite directions. Table 4 represents a summary of the displacement vector of rain motion based on motion tracking analysis using The PLKOF method.

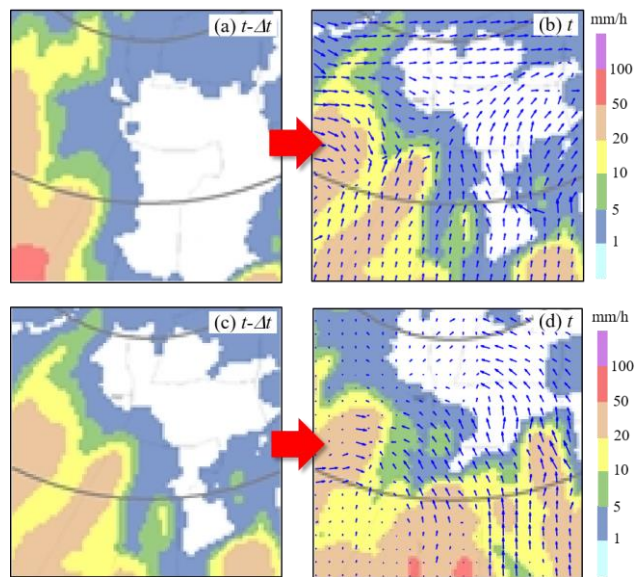


**Figure 6** Example of motion vector estimations on November 10<sup>th</sup>, 2016 at (a) 14:20 (b) 14:30 with displacement vector (C) 14:30 (d) 14:00 with displacement vector

Based on Table 4 the rain motion displacement averagely shows values about 9 pixels or equal to 8.3 km/h in velocity. However, some parts in the domain have relatively large displacement values, especially in events such as R5, R6, R7, and R9, where maximum displacement exceeds the domain area. Refers to Ulbrich et al. [43], the advection of rainfall objects can reach a maximum velocity of 130 km/h. With a pixel size of 150 x 150 meters, such velocity is equivalent to 144 pixels in 10 minutes, while the

domain area is limited to 100x100 pixels only. Such large displacement as identified in several cases above generally occurs due to the growth and decay activities.

**Table 4** Summary of the displacement vector of rain motion

Rainfall events	Average Displacements		Dominant directions	Predictability indexes		
	(pixels)	velocity (km/h)		POD	CSI	FAR
R1	4	3.6	NE	0.882	0.801	0.104
R2	7	6.3	NE	0.957	0.920	0.046
R3	5	4.5	NE, SE	0.883	0.792	0.147
R4	8	7.2	NE	0.791	0.684	0.163
R5	13	11.7	NE	0.768	0.655	0.220
R6	8	7.2	NE	0.813	0.703	0.186
R7	11	9.9	N, E, NE, SE, SW	0.740	0.538	0.379
R8	6	5.4	NE	0.916	0.735	0.245
R9	21	18.9	NE, NW	0.706	0.571	0.300

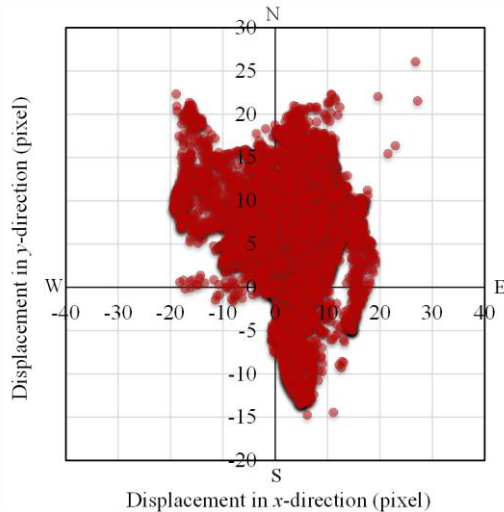


**Figure 7** Scatter plot of displacement vector estimations on November 10<sup>th</sup>, 2016, at 14:20-14:30

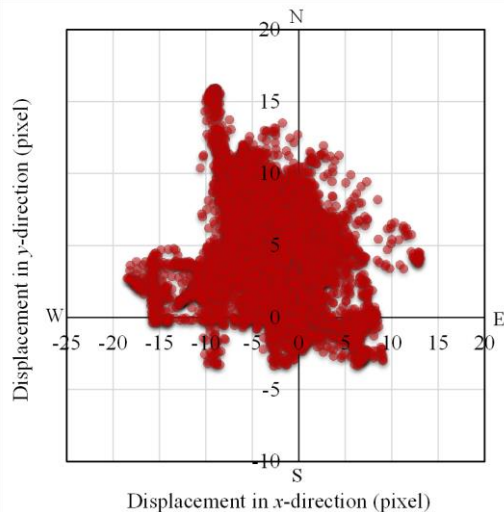


**Figure 8** Scatter plot of displacement vector estimations on November 10<sup>th</sup>, 2016, at 14:30-14:40

In general, the algorithm used for rain motions tracking shows good results, especially for small displacements. The overall performance of HPLK model is generally satisfied, especially of its ability to predict the rain cell displacements as indicated by the POD, CSI, and FAR indexes (Table 4). The average values of POD and CSI were 0.882 and 0.801, respectively, while the FAR was 0.104. The POD and CSI index values averagely decreased while FAR increased at the end of the simulation sequences. However, the algorithm cannot identify the occurrence of rain growth and decay, so the situation is considered as an extremely rapid rain motion from or to the outside domain area. As a consequence, a critical error occurs when estimating the displacement of rain motion field. For example, it arises in the rainfall event of October 8<sup>th</sup>, 2017, where there are very irrational displacement values as shown in Figure 9. This case happens due to the algorithm detects the growth of rain objects (Figure 10) as a swift movement from outside of the domain area.

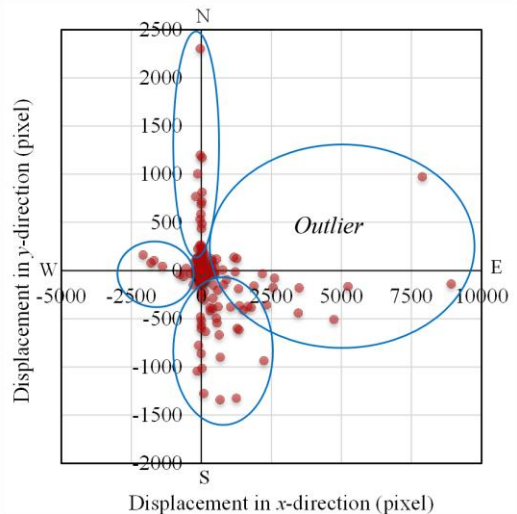


**Figure 9** Scatter plot of displacement vector estimations error on October 8<sup>th</sup>, 2017, 17:50-18:00

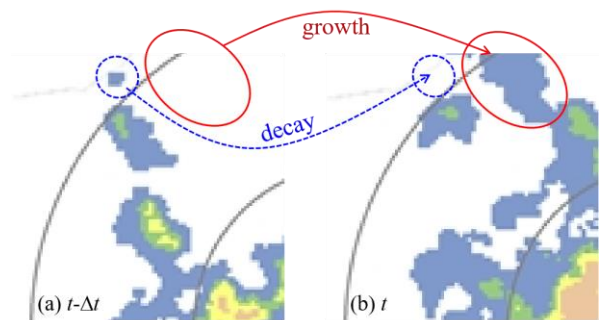


**Figure 10** The growth and decay of rain objects detection from two consecutive images on October 8<sup>th</sup>, 2017, at (a) 17:50 and (b) 18:00

The shortcoming of objects tracking with the optical flow has been revealed by Bechini and Chandrasekar [13], where rain motions detected based on existing objects, irrespective the occurrence of rain growth and decay. Also, the displacement vector of rain motion is usually estimated from observations confined to the radar domain. There was no simple model that could complement the lack of optical flow method. An enhanced optical flow technique proposed by [13] was too complex and involved many parameters.

To evaluate the success performance of the proposed model, we attempt to compare the values of the evaluation indexes toward PPLK model (Liu, *et al.*, 2015) and the SPLK model (Li, *et al.*, 2018). The comparison is shown in Figure 11. Based on Figure 11, the PLKOF model in this study is superior to the PPLK model for POD, CSI and FAR indexes with an advantage of 11%, 15% and -14%, respectively. Compared to the SPLK model, the CSI index has almost the same value, but the SPLK model is slightly superior for the POD and FAR values.

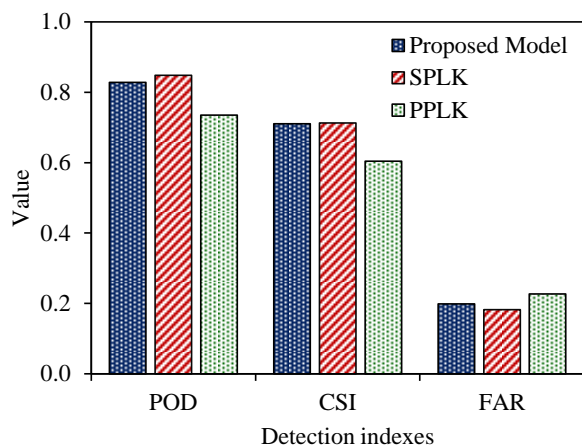


**Figure 11** Comparison of POD, CSI and FAR index values between the Proposed Models, PPLK, and SPLK

#### 4.0 CONCLUSION

In this study, the PLKOF method was applied to analyze displacement vector of rain motions using high-resolution X-band MP radar image data. The use of high-resolution image data with a grid size of 150x150 m is very worthwhile because the displacement of rain motions in the sub-pixel scale assumed to be small, and it can be ignored. Simulation results show that this method is relatively good at detecting small displacements or slow movement. The ability of PLKOF method in rain position predictability at time  $t+\Delta t$  is satisfied as indicated by the POD, CSI, and FAR indexes. From the nine selected rainfall events, the average displacement of 10-minutes time interval rain motions in the Mt. Merapi region is 9 pixels (8.3 km/h) with the dominant direction being northeast.

We emphasized that the occurrence of rain growth and decay are the main problem that still cannot be resolved with the PLKOF method in this study. This method does not consider the presence of such scheme, so the algorithm takes into account the new object as a displacement from or to an area outside the observation domain with very high velocity. Further investigation to overcome such problems is necessary for the development of better algorithms. In the future works, simulations with more cases are needed to train models with varies data that represent the study area. Moreover, the experiment of applying several image filtering parameters or even filtering methods would also provide an optimal result to enhance the performance of the PLKOF method.

#### Acknowledgement

This publication was supported by Faculty of Engineering, Bangka Belitung University. The authors would like to express their gratitude to the JST/JICA - SATREPS and Hydraulic Laboratory of Civil and Environmental Engineering Department, Universitas Gadjah Mada for the provision of access to the data, Mr. Gilang and Mr. Bobby for their invaluable support of this research.

#### References

- [1] Otani, K., Legono, D., Darsono, S., and Suharyanto. 2018. Effects of Disaster Management Programs on Individuals' Preparedness in Mount Merapi. *Journal of the Civil Engineering Forum*. 4(1): 79-90. <https://doi.org/10.22146/jcef.29580>.
- [2] Lavigne, F., Thouret, J. C., Voight, B., Suwa, H., and Sumaryono, A. 2000. Lahars at Merapi Volcano, Central Java: An Overview. *Journal of Volcanology and Geothermal Research*. 100: 423-456. [https://doi.org/10.1016/S0377-0273\(00\)00150-5](https://doi.org/10.1016/S0377-0273(00)00150-5).
- [3] Hambali, R., Legono, D., Jayadi, R., and Oishi, S. 2018. Statistical Properties of Short-term Rainfall Time Series as Observed by XMP Radar (Case of Mt. Merapi Area). *Proceeding of 21st IAHR-APD Congress 2018*. 1317-1324.
- [4] Fathani, T. F., and Legono, D. 2013. The Application of Monitoring and Early Warning System of Rainfall-Triggered Debris Flow at Merapi Volcano, Central Java, Indonesia. In *Progress of Geo-Disaster Mitigation Technology in Asia*. Heidelberg: Springer Berlin Heidelberg. 263-275. [https://doi.org/10.1007/978-3-642-29107-4\\_13](https://doi.org/10.1007/978-3-642-29107-4_13).
- [5] Fibriyanto, E. A. 2015. Development of Warning Criteria for Lahar Flow Disaster in Gendol River Area of Mount Merapi. *Journal of the Civil Engineering Forum*. 1(1): 17-22. <https://doi.org/10.22146/jcef.22726>.
- [6] Van Hone, M. P. 2003. *Short-Term Precipitation Nowcasting for Composite Radar Rainfall Fields*. Massachusetts Institute of Technology.
- [7] Zahraei, A., Hsu, K., Sorooshian, S., Gourley, J. J., Hong, Y., and Behrang, A. 2013. Short-Term Quantitative Precipitation Forecasting Using an Object-based Approach. *Journal of Hydrology*. 483: 1-15. <https://doi.org/10.1016/j.jhydrol.2012.09.052>.
- [8] Ganguly A. R., and Bras, R. L. 2003. Distributed Quantitative Precipitation Forecasting Using Information

- from Radar and Numerical Weather Prediction Models. *Journal of Hydrometeorology*. 4: 1168-1180. [https://doi.org/10.1175/1525-7541\(2003\)004<1168:DQPFUI>2.0.CO;2](https://doi.org/10.1175/1525-7541(2003)004<1168:DQPFUI>2.0.CO;2).
- [9] Liu, Y., Xi, D., Li, Z., and Hong, Y. 2015. A New Methodology for Pixel-Quantitative Precipitation Nowcasting Using a Pyramid Lucas Kanade Optical Flow Approach. *Journal of Hydrology*, 529: 354-364. <https://doi.org/10.1016/j.jhydrol.2015.07.042>.
- [10] Golding, B. W. 1998. Nimrod: A System for Generating Automated Very Short Range Forecasts. *Meteorological Applications*. 16: 1-16. <https://doi.org/10.1017/S1350482798000577>.
- [11] Wang, P., Smeaton, A., Lao, S., Connor, E. O., Ling, Y., and Connor, N. O. 2009. *Short-Term Rainfall Nowcasting: Using Rainfall Radar Imaging*. Eurographics Ireland.
- [12] Zahraei, A., Hsu, K., Sorooshian, S., Gourley, J. J., Lakshmanan, V., Hong, Y., and Bellerby, T. 2012. Quantitative Precipitation Nowcasting: A Lagrangian Pixel-Based Approach. *Atmospheric Research*. 118: 418-434. <https://doi.org/10.1016/j.atmosres.2012.07.001>.
- [13] Bechini R., and Chandrasekar, V. 2017. An Enhanced Optical Flow Technique for Radar Nowcasting of Precipitation and Winds. *Journal of Atmospheric and Oceanic Technology*. 34: 2637-2658. <https://doi.org/10.1175/JTECH-D-17-0110.1>.
- [14] Chu, H., Liu, M., Sun, M., and Chen, L. 2018. Rainfall Nowcasting by Blending of Radar Data and Numerical Weather Prediction [Online First]. *Numerical Analysis and Prediction for Meteorological and Atmospheric Systems*. Shanghai, China: IntechOpen. 1-18. <https://doi.org/10.5772/intechopen.81632>.
- [15] Van Horne, M. P., Vivoni, E. R., Entekhabi, D., Hoffman, R. N., and Grassotti, C. 2006. Evaluating the Effects of Image Filtering in Short-term Radar Rainfall Forecasting for Hydrological Applications. *Meteorological Applications*. 13: 289-303. <https://doi.org/10.1017/S1350482706002295>.
- [16] Li, L., He, Z., Chen, S., Mai, X., Zhang, A., Hu, B., Li, Z., and Tong, X. 2018. Subpixel-Based Precipitation Nowcasting with the Pyramid Lucas – Kanade Optical Flow Technique. *Atmosphere*. 9(260): 1-22. <https://doi.org/10.3390/atmos9070260>.
- [17] Grecu M., and Krajewski, W. F. 2000. A Large-Sample Investigation of Statistical Procedures for Radar-Based Short-Term Quantitative Precipitation Forecasting. *Journal of Hydrology*. 239: 69-84. [https://doi.org/10.1016/S0022-1694\(00\)00360-7](https://doi.org/10.1016/S0022-1694(00)00360-7).
- [18] Germann U., and Zawadzki, I. 2002. Scale-Dependence of the Predictability of Precipitation from Continental Radar Images. Part I: Description of the Methodology. *Monthly Weather Review*. 130(4): 2859-2873. [https://doi.org/10.1175/1520-0493\(2002\)130<2859:SDOTPO>2.0.CO;2](https://doi.org/10.1175/1520-0493(2002)130<2859:SDOTPO>2.0.CO;2).
- [19] Montanari, L., Montanari, A., and Toth, E. 2006. A Comparison and Uncertainty Assessment of System Analysis Techniques for Short-term Quantitative Precipitation Nowcasting Based on Radar Images. *Journal of Geophysical Research*. 111(D14111): 1-12. <https://doi.org/10.1029/2005JD006729>.
- [20] Berenguer, M., Sempere-torres, D., and Pegram, G. G. S. 2011. SBMcst – An Ensemble Nowcasting Technique to Assess the Uncertainty in Rainfall Forecasts by Lagrangian Extrapolation. *Journal of Hydrology*. 404(3-4): 226-240. <https://doi.org/10.1016/j.jhydrol.2011.04.033>.
- [21] Woo, W., and Wong, W. 2017. Operational Application of Optical Flow Techniques to Radar-based Rainfall Nowcasting. *Atmosphere*. 8(48): 1-20. <https://doi.org/10.3390/atmos8030048>.
- [22] Bowler, N. E. H., Pierce, C. E., and Seed, A. 2004. Development of a Precipitation Nowcasting Algorithm Based Upon Optical Flow Techniques. *Journal of Hydrology*. 288: 74-91. <https://doi.org/10.1016/j.jhydrol.2003.11.011>.
- [23] Cheung P., and Yeung, H. Y. 2012. Application of Optical-Flow Technique to Significant Convection Nowcast for Terminal Areas in Hong Kong. *The 3rd WMO International Symposium on Nowcasting and Very Short-Range Forecasting*. 1-10.
- [24] Park, S.-G., Maki, M., Iwanami, K., Bringi, V. N., and Chandrasekar, V. 2005. Correction of Radar Reflectivity and Differential Reflectivity for Rain Attenuation at X Band. Part II: Evaluation and Application. *Journal of Atmospheric and Oceanic Technology*. 22(11): 1633-1655. <https://doi.org/10.1175/JTECH1804.1>.
- [25] Hambali, R., Legono, D., Jayadi, R., and Oishi, S. 2019. Improving Spatial Rainfall Estimates at Mt. Merapi Area Using Radar-Rain Gauge Conditional Merging. *Journal of Disaster Research*. 14(1): 69-79. <https://doi.org/10.20965/jdr.2019.p0069>.
- [26] B. K. P. Horn and B. G. Schunck. 1981. Determining Optical Flow. *Artif. Intell.* 17: 185-203. [https://doi.org/10.1016/0004-3702\(81\)90024-2](https://doi.org/10.1016/0004-3702(81)90024-2).
- [27] Gibson, J. J. 1950. *The Perception of the Visual World*. Boston: The Riverside Press, Cambridge.
- [28] Tauro, F., Tosi, F., Mattoccia, S., Toth, E., Piscopia, R., and Grimaldi, S. 2018. Optical Tracking Velocimetry (OTV): Leveraging Optical Flow and Trajectory-based Filtering for Surface Streamflow Observations. *Remote Sensing*. 10(12): 1-24. <https://doi.org/10.3390/rs10122010>.
- [29] Lenzano, M. G., Lannutti, E., Toth, C., Rivera, A., and Lenzano, L. 2018. Detecting Glacier Surface Motion by Optical Flow. *Photogrammetric Engineering & Remote Sensing*. 84(1): 33-42. <https://doi.org/10.14358/PERS.84.1.33>.
- [30] Urbich, I., Bendix, J., and Müller, R. 2018. A Novel Approach for the Short-term Forecast of the Effective Cloud Albedo. *Remote Sensing*. 10(95): 1-16. <https://doi.org/10.3390/rs10060955>.
- [31] Hadhri, H., Vernier, F., Atto, A. M., and Trouvé, E. 2019. Time-lapse Optical Flow Regularization for Geophysical Complex Phenomena Monitoring. *ISPRS Journal of Photogrammetry and Remote Sensing*. 150: 135-156. <https://doi.org/10.1016/j.isprsjprs.2019.02.007>.
- [32] Ayzel, G., Heistermann, M., and Winterrath, T. 2019. Optical Flow Models as an Open Benchmark for Radar-based Precipitation Nowcasting (rainymotion v0.1). *Geoscientific Model Development*. 12(4): 1387-1402. <https://doi.org/10.5194/gmd-12-1387-2019>.
- [33] Fleet D. J., and Weiss, Y. 2005. Optical Flow Estimation. In *Mathematical Models in Computer Vision: The Handbook*. Springer. 239-258.
- [34] O'Donovan, P. 2005. *Optical Flow: Techniques and Applications*. The University of Saskatchewan.
- [35] Xue, T., Mobahi, H., and Freeman, W. T. 2015. The Aperture Problem for Refractive Motion. *2015 IEEE Conference on Computer Vision and Pattern Recognition (CVPR)*. 3386-3394. <https://doi.org/10.1109/CVPR.2015.7298960>.
- [36] Ravisankar, P., Sharmila, T. S., and Rajendran, V. 2018. Acoustic Image Enhancement Using Gaussian and Laplacian Pyramid – A Multiresolution Based Technique. *Multimedia Tools and Applications*. 77(5): 5547-5561. <https://doi.org/10.1007/s11042-017-4466-7>.
- [37] Dash S., and Jena, U. R. 2017. Gaussian Pyramid Based Laws' Mask Descriptor for Texture Classification. In *2017 International Conference on Wireless Communications. Signal Processing and Networking (WISPNET)*. 654-658. <https://doi.org/10.1109/WISPNET.2017.8299841>.
- [38] Li, S., Hao, Q., Kang, X., and Benediktsson, J. A. 2018. Gaussian Pyramid Based Multiscale Feature Fusion for Hyperspectral Image Classification. *IEEE Journal of Selected Topics in Applied Earth Observation and Remote Sensing*. 11(9): 3312-3324. <https://doi.org/10.1109/JSTARS.2018.2856741>.

- [39] Barron, J. L., Fleet, D. J., and Beauchemin, S. S. 1994. Performance of Optical Flow Techniques. *International Joint Conference of Computer Vision*. 43-77. <https://doi.org/10.1007/BF01420984>.
- [40] Konlambigue, S., Pothin, J.-B., Honeine, P., and Benschair. 2018. Fast and Accurate Gaussian Pyramid Construction by Extended Box Filtering. *26<sup>th</sup> European Signal Processing Conference (EUSIPCO)*. 400-404. <https://doi.org/10.23919/EUSIPCO.2018.8553321>.
- [41] Karpushin, M., Valenzise, G., and Dufaux, F. 2016. An Image Smoothing Operator for Fast and Accurate Scale Space Approximation. *IEEE International Conference on Acoustics, Speech, and Signal Processing*. <https://doi.org/10.1109/ICASSP.2016.7471999>.
- [42] Neustaedter, C. 2002. An Evaluation of Optical Flow Using Lucas and Kanade's Algorithm. [Online]: <http://clab.iat.sfu.ca/pubs/EvaluatingLucasKanade.pdf>.
- [43] Ulbrich, U., Fink, A. H., Klawns, M., and Pinto, G. 2001. Three Extreme Storms over Europe in December 1999. *Weather*. 56: 70-80. <https://doi.org/10.1002/j.1477-8696.2001.tb06540.x>.